Actin crosslinker competition and sorting drive emergent GUV size-dependent actin network architecture

Yashar Bashirzadeh[1], Steven A. Redford[2,3], Chatipat Lorpaiboon[4], Alessandro Groaz[1,*], Thomas Litschel[5], Petra Schwille[5], Glen M. Hocky[6], Aaron R. Dinner[2,4], Allen P. Liu[1,7,8,9]

[1] Department of Mechanical Engineering, University of Michigan, Ann Arbor, Michigan, 48109, USA

[2] James Franck Institute, University of Chicago, Chicago, IL, USA

[3] The graduate program in Biophysical Sciences, The University of Chicago, Chicago, Illinois, 60637, USA

[4] Department of Chemistry, University of Chicago, Chicago, IL, 60637, USA

[5] Department of Cellular and Molecular Biophysics, Max Planck Institute of Biochemistry, 82152, Martinsried, Germany

[6] Department of Chemistry, New York University, New York, NY, 10016, USA

[7] Department of Biomedical Engineering, University of Michigan, Ann Arbor, Michigan, 48109, USA

[8] Department of Biophysics, University of Michigan, Ann Arbor, Michigan, 48109, USA

[9] Cellular and Molecular Biology Program, University of Michigan, Ann Arbor, Michigan, 48109, USA

* Current address: Department of Neuroscience, Baylor College of Medicine, Houston, Texas, , 77030, USA

Corresponding author:

A.P.L: allenliu@umich.edu; 2350 Hayward Street, University of Michigan, Ann Arbor, Michigan 48109. Tel: +1 734-764-7719.

Abstract

Robust spatiotemporal organization of cytoskeletal networks is crucial, enabling cellular processes such as cell migration and division. α-Actinin and fascin are two actin crosslinking proteins localized to distinct regions of eukaryotes to form actin bundles with optimized spacing for cell contractile machinery and sensory projections, respectively. *In vitro* reconstitution assays and coarse-grained simulations have shown that these actin bundling proteins segregate into distinct domains with a bundler size-dependent competition-based mechanism, driven by the minimization of F-actin bending energy. However, it is not known how physical confinement imposed by the cell membrane contributes to sorting of actin bundling proteins and the concomitant reorganization of actin networks in intracellular environment. Here, by encapsulating actin, α-actinin, and fascin in giant unilamellar vesicles (GUVs), we show that the size of such a spherical boundary determines equilibrated structure of actin networks among three typical structures: single rings, astral structures, and star-like structures. We show that α-actinin bundling activity and its tendency for clustering actin is central to the formation of these structures. By analyzing physical features of crosslinked actin networks, we show that spontaneous sorting and domain formation of α-actinin and fascin are intimately linked to the resulting structures. We propose that the observed boundary-imposed effect on sorting and structure formation is a general mechanism by which cells can select between different structural dynamical steady states.

The spatial organization of the cytoskeleton is critically important for coordinating forces that enable a cell to move, change shape, and organize intracellular movements[1, 2]. Filamentous actin (F-actin) with the help of actin binding proteins and in close cooperation with other cytoskeletal components controls the mechanics of eukaryotes during migration, division, vesicular traffic, and other major cellular processes. Among functionally diverse actin binding proteins, actin crosslinkers drive the assembly and spatiotemporal organization of morphologically and functionally distinct actin networks throughout the cell. Given the diversity of actin binding proteins and an array of different actin crosslinkers, a fundamental question is how different actin crosslinkers are organized into emergent mesoscopic structures.

α-Actinin is one of the key actin crosslinkers found in contractile units, particularly in actin stress fibers of migrating cells, and plays a role in modulating actomyosin reorganization and contraction. It also intensely localizes to and participates in the assembly of actomyosin contractile rings to drive membrane movements associated with yeast cytokinesis[3]. Recent evidence has shown that α-actinin aggregates at the entry site of Human Immunodeficiency Virus (HIV) to $CD4^+$ T cells in order to regulate actin cortex rearrangements during membrane fusion, making α-actinin a potential target for antiviral therapy[4]. Fascin, another key actin crosslinker, on the other hand, is predominantly present at the cell leading edge. There, fascin tightly bundles actin to deform the membrane, forming sensory protrusions such as filopodia. In metastatic cancer cells, invadopodia that consist of fascin-bundled actin can also protrude into the extracellular matrix[5, 6].

It has been shown in fission yeast that competition of monomeric actin with assembly factors directly controls Arp2/3 complex-mediated vs. formin-mediated actin nucleation[7]. This idea led to subsequent studies showing that competition-based mechanisms can drive sorting of actin binding proteins to distinct actin filament networks[8]. Polymerized actin in the presence of Arp2/3 complex *in vitro* transitioned into star-like structures in the presence of fascin, which possibly bundles F-actin remote from Arp2/3 complex-rich star core[9]. Actin crosslinking proteins not only are segregated to different parts of the actin cytoskeleton but are also critical in determining the localization of other actin binding proteins. α-Actinin dimers are about 35 nm long and form anti-parallel actin bundles with perfect spacing for myosin binding and contraction of actin networks. On the other hand, fascin is a short monomer capable of forming parallel, aligned, packed and rigid actin bundles with about 6 nm spacing. Biomimetic motility assays with branched

actin networks reconstituted on polystyrene beads formed bundled filaments in the presence of fascin to propel beads and form filopodia-like bundles in the shape of star-like patterns[10, 11]. Using a similar experimental system, in the presence of both α-actinin and fascin, branched actin networks formed star-like patterns and spontaneously segregated into distinct domains where α-actinin is localized near the surface of the beads, and fascin is localized in thin star-like spikes[10, 12]. *In vitro* sedimentation and bulk actin bundling assays showed that cooperative and bundler size-dependent competitive binding effects of α-actinin and fascin can spontaneously drive their sorting and influence the association of other actin binding proteins[12]. Theoretical models of 2-filament actin bundling in 2D by using coarse-grained simulations and further experimental evidence revealed that energetic cost of F-actin bending modulates size-dependent sorting of α-actinin and fascin, and that single-filament binding kinetics and actin polymerization rate influence the domain length of each crosslinker before reaching equilibrium[13].

Although open biomimetic platforms such as supported lipid bilayers, lipid-coated beads, and surface of GUVs introduce appropriate boundary conditions for self-assembly of cytoskeletal components into biochemically and mechanically functional networks[14, 15, 16, 17, 18, 19], they do not impose and demonstrate the influence of confined environment of the cell on network organization. To this end, protein components have been encapsulated within or attached to inside lipid-coated single emulsion droplets or GUVs[20, 21, 22, 23, 24]. Encapsulated microtubule-kinesin networks in droplets, for instance, reorganized into ring-like, cortical, or star-like structures based on droplet size[25, 26]. Co-assembly of microtubules and branched actin from *Xenopus* egg extracts in droplets resulted in their co-alignment and the formation of star-like actin networks[27]. Constrained by branched actin networks, the mobility of the poles of star-like microtubules was modulated by actomyosin contraction[27]. In order to minimize filament elastic energy, actin filaments encapsulated in cell-sized confinement with a radius greater than filament persistence length merged into peripheral actin rings in the presence of a crowding agent methylcellulose or bundling proteins[24, 28]. Myosin motors, in these networks, were shown to promote the assembly of a single contractile ring[28]. However, strong actomyosin contraction can induce the formation of aggregates at the center of large droplets or at the periphery of small droplets[29]. These studies highlight the intrinsic features of actin binding proteins that drive self-organization of F-actin into functional connective networks.

Motor proteins can drive organization of actin networks in confined systems and passive crosslinkers need a nucleation surface to have a large-scale actin organization behavior. It is not clear whether passive crosslinkers in a membrane-enclosed environment can generate mesoscopic actin structures. Here, we encapsulate monomeric actin with α-actinin and fascin in a spherically confined environment of GUVs. We analyze the influence of GUV size and crosslinker concentration on the structural organization of confined actin networks. We identify actin crosslinker competition and sorting in encapsulated actin networks as factors that drive emergent GUV size-dependent actin network organization. We show that α-actinin crosslinking activity, without any need for motor-driven contraction, induces clustering of actin to a focal region which is critical for the formation of central star-like patterns by network connectivity and protein sorting in large GUVs. This bottom-up approach shows that biochemical and physical characteristics of actin, α-actinin, and fascin bounded within a membrane are sufficient for self-organization and domain formation of actin networks without the need for complex cell signaling and machinery.

Encapsulated α-actinin and fascin together form distinct actin network architectures.

In order to investigate actin network architecture in confinement, we encapsulated α-actinin and fascin together with actin inside GUVs, using a modified continuous droplet interface crossing encapsulation (cDICE)[24, 30] approach. Actin structures were 3D 'skeletonized' from *z*-stack confocal image sequences of actin using an ImageJ-SOAX[31, 32]-MATLAB-based processing tool (see Methods and **Supplementary Figs. S1 and S2**). This enabled visualization and characterization of actin networks under various conditions. Co-encapsulation of α-actinin and fascin together with actin resulted in the formation of distinct actin structures **(Fig. 1)**. A single actin bundle in GUVs appeared as an actin ring around the GUV periphery. Multi-bundles of actin, however, appeared as arrays of long bundled filaments emanating from actin aggregates **(Fig. 1,** white arrows**)** resembling astral structures. Actin aggregates were often detectable on single actin rings as well. Actin aggregates localized at either the GUV periphery or GUV center, in the latter case, forming the center of a star-like structure **(Fig. 1**, yellow arrow**)**. Aster-like structures with peripheral aggregates will be referred to as 'aster-like' and aster-like structures with central aggregates will be referred to as 'star-like' in the rest of this work. Furthermore, aster-like structures could form partial or complete rings around the GUV periphery; whereas in star-like

structures, most of the actin bundles that were extended towards the GUV periphery appeared nearly straight.

Large bending rigidity of α-actinin-fascin-actin bundles in actin rings and asters could cause GUV shape changes which is attributable to fascin bundling activity. As anticipated, fascin, in the absence of α-actinin, formed rigid actin bundles and stably deformed GUVs instead of bending by the confined membrane **(Supplementary Fig. S3)**. Fascin alone did not induce F-actin aggregation nor did it result in the formation of actin structures observed when α-actinin and fascin were co-encapsulated. Following the observations that encapsulated actin in the presence of α-actinin and fascin form distinct structures and that fascin, without teaming up with α-actinin, does not shape the observed structures, we asked whether 1) anti-parallel bundling by α-actinin shapes these structures or 2) a cooperation/competition among the crosslinkers modulates self-assembly.

The formation of complex structures with actin aggregates in the absence of motor proteins was surprising, as motor-driven dynamics is required for F-actin clustering[33, 34]. However, simulations have shown that confined actin and crosslinkers can form rings, open bundles, irregular loops or aggregates depending on crosslinker type and concentration, and confinement geometry[35]. Although α-actinin and fascin have similar bundling affinities, α-actinin has a higher binding affinity to single filaments and forms antiparallel bundle with large spacing and mixed polarity as opposed to unidirectional packed parallel bundling by fascin. These properties enables α-actinin to form more complex structures in bulk including bundle clusters at high α-actinin concentrations[36, 37]. *In vitro* reconstitution and simulation studies have also shown that the actin contractile machinery in eukaryotes is a result of one or a combination of three distinct coordinating mechanisms, F-actin buckling in disordered actomyosin networks, sliding (sarcomere-like contraction), and polarity sorting[35, 38, 39, 40, 41, 42, 43]. All three mechanisms are promoted by α-actinin and the polarity sorting and buckling mechanisms can result in myosin-driven clustering and the formation of large star-like structures[39, 40, 41]. The average number of F-actin connectors such as Arp2/3 complex and α-actinin per actin filament (network connectivity) can regulate and determine the mechanism of contraction in actomyosin networks[41, 42]. Actin bundling by α-actinin was shown to induce the contraction of micropatterned disordered actomyosin bundle rings[41]. This underscores the importance of network connectivity by α-actinin in regulating actin network contraction and possibly aggregation. In reconstituted actomyosin

networks on circular micropatterns, contraction induced the formation of star-like patterns and the presence of α-actinin resulted in centering of the star-like patterns[44]. α-actinin also mediated droplet-size-dependent cluster localization of encapsulated actomyosin networks[45]. In cells geometrically confined on micropatterned substrates, α-actinin was shown to modulate symmetric actomyosin-driven centering[44]. Hence, α-actinin-regulated network connectivity and the possibility of a GUV size-dependent clustering directed us to explore the role of confinement and α-actinin-mediated self-organization in aggregation and architecture of actin assemblies.

α-Actinin is responsible for aggregation and GUV size-dependent formation of actin rings and asters.

In order to examine the function of α-actinin in the architecture of actin bundles, we encapsulated actin and α-actinin at various molar ratios in GUVs with a large range of diameters. In the presence of only α-actinin, actin bundle architecture was highly dependent on GUV size, manifesting the impact of spherical confinement on bundle curvature and bundle-bundle interactions **(Fig. 2a-b)**. Based on the tendency of actin bundles to bend around the membrane, we observed three typical geometries: single actin rings, distinct yet connected actin bundles with no rings (networks), or a combination of connected actin bundles including actin ring(s) around the periphery (ring/network structures). The probability of single-ring formation and network formation as a function of GUV size at different α-actinin concentrations is shown in **Figure 2c-d**. Large membrane curvature and low volume of small GUVs caused α-actinin-bundled actin to merge into a single ring (**Fig. 2c)**, similar to what has been reported previously[24, 28]. Increasing α-actinin beyond 1:10 molar ratio tended to negatively affect actin ring formation. The probabilities of actin bundles forming a single ring in small (7-12 μm diameter) GUVs were high (99% (1:10), 90% (2:10), 88% (3:10)). The probabilities of the formation of single rings in medium (12-16 μm diameter) GUVs dropped significantly (56% (1:10), 54% (2:10), 41% (3:10)), and the probabilities further decreased in large (> 16 μm) GUVs (19% (1:10), 4% (2:10), 1% (3:10)). Characterization of actin rings in small and medium GUVs showed that actin rings slightly deviate from a perfect circle at GUV midplane (a plane passing GUV center) **(Supplementary Fig. S4a-c)**. All actin rings in small GUVs were formed in a close proximity to the membrane (**Supplementary Fig. S4a**) and ring arc length ranged between 0.8-0.85 GUV circumference (**Supplementary Fig. S4c**). These signify ring formation near GUV midplane. Experimental and numerical evidence shows

that upon compression, rings can assemble in the equatorial plane perpendicular to the direction of compression[28, 35]. As the GUV size increased, we found more complex actin network geometries (**Fig. 2d)**, as the formation of actin rings was reduced. Some actin structures appeared as a combination of ring/networks. The probabilities of network formation in small GUVs were low (0% (1:10), 0% (2:10), 6% (3:10)). The probabilities of network formation in medium GUVs slightly increased (1% (1:10), 5% (2:10), 25% (3:10)), while the increase was significant in large GUVs (20% (1:10), 33% (2:10), 63% (3:10)). In GUVs greater than 40 μm in diameter, more actin bundles behaved as flexible polymers forming networks in the lumen away from the membrane (**Fig. 2a)**. This suggests that the architecture of actin bundles confined in a large GUV does not rely on direct bundle-membrane interaction. It should be emphasized, however, that single actin rings could occasionally form in the periphery of large GUVs **(Supplementary Fig. S5, white arrows)**.

Compared to fascin-only bundled actin, actin bundled only by α-actinin displayed a richer set of phenotypes when assembled inside GUVs, and we suspect actin aggregates that we observed in α-actinin-fascin-actin networks may be attributed to α-actinin. In the majority of medium and large GUVs regardless of α-actinin concentration, F-actin aggregated to a focal point at the GUV periphery (**Fig. 3a, arrows)**. It should be emphasized that not all crosslinked networks in large GUVs formed aggregates **(Supplementary Fig. S5, red arrows)**. At only high α-actinin concentrations, we frequently observed large aggregates proximal to the membrane (**Fig. 3b-c)**. Previously, a mathematical model showed that the competition between stochastic interaction of contractile networks with lipid membrane and network contraction-dependent hydrodynamic forces determine aggregate localization in droplets[29]. Experimental evidence showed that smaller droplets increase the chance of transient network engagement/disengagement to the membrane thereby keeping aggregates near the periphery[29]. Before reaching structural equilibrium and stabilization **(Supplementary Fig. S6a-b)**, encapsulated α-actinin-bundled actin in our experiments could initially change shape **(Supplementary Fig. S6c)**. This signifies the absence of specific interactions between actin bundles and lipid bilayer. It should be noted that photo-bleaching of fluorophores significantly impaired actin network self-assembly at the early stages of actin bundling in GUVs. This prevented us from capturing the dynamics of self-assembly by z-stack imaging at a high-temporal resolution. A model based on percolation theory and experimental evidence showed that the presence of extra α-actinin increases the probability of

actomyosin bridge formation with lipid monolayer-coated droplets acting against center-directed actomyosin waves, and this results in edge-positioning of actomyosin clusters[45]. Replacing phospholipids in the droplet membrane with a PEG-based surfactant was found to reduce protein-membrane interaction and thereby reducing the probability of aggregate localization at the droplet periphery[45]. Since we did not find any sign of specific binding between non-contractile bundles and phospholipids, it is likely that transient attractive forces between α-actinin-actin complex with the lipid bilayer position the aggregates at the periphery. This is followed by bending of bundles around the membrane away from the focal point to minimize elastic energy thereby shaping the aster-like structures. Majority of actin bundles (~60%) in large GUVs indeed formed aster-like structures, irrespective of α-actinin concentration (**Fig. 3d)**. Among the large GUVs that have asters, the fraction of GUVs in which all bundles elongated entirely around the GUV periphery, as opposed to localized to the lumen, increased with α-actinin concentration (**Fig. 3e)**. Size-dependent structures formed by α-actinin-actin bundles are summarized schematically in **Figure 3f**. Although we observed α-actinin-actin aggregates, similar to what we reported in the α-actinin-fascin-actin condition earlier, we rarely saw α-actinin-actin aggregates in the lumen or star-like structures in the α-actinin-actin condition. This implies that additional mechanisms are involved in multi-crosslinker-mediated formation of star-like structures in our encapsulated system.

A simulation framework reveals the formation of star-like structures in the presence of α-actinin and fascin.

To understand the microscopic origin of pattern formation in α-actinin-fascin-actin assemblies we turned to coarse-grained simulations of cytoskeletal dynamics modeling filaments by using beads and springs. We began by parameterizing the representations of "α-actinin" and "fascin" in the simulation by comparing the structures resultant from each alone in simulation with similar structures from experiments. As in the experiments, fascin in simulation produces tight, defined bundles while α-actinin exhibits a greater degree of branching (**Fig. 4a-b**). We next combined the two at either a one to one or three to one ratio of "α-actinin" to "fascin". We found that the structures of networks simulated with these two different ratios bear a striking resemblance to star-like structures seen in the experiments (**Fig 4c-d**). Furthermore, we varied the concentration ratio of "α-actinin" and "fascin" and found that the actin probability density function (PDF) at 1:1

ratio is peaked at the center and consistently decays as the distance from the center of the simulation box increases, whereas the PDF at 3:1 ratio remains flat for some distance from the center **(Fig. 4e-f,** yellow region**)**. We began to understand how divergent structures arise by examining the course of the simulation. When we examine the root-mean-square distance (RMSD) of each actin bead from its initial position to its position in the final structure, we find that the filaments in the 3:1 case move less than those in the 1:1 (**Fig. 4g**). This reduction in mobility is accompanied by a corresponding increase in the amount of potential energy stored in the bending of actin filaments in the simulation (**Fig. 4f**). Together these observations suggest that the additional α-actinin in the 3:1 case, due to its permissive binding range, may be trapping the filaments in a bent conformation before they are able to relax into lower energy linear bundles. This idea is further supported by the finding that shorter filaments rearrange less, resulting in a less delocalized actin center in the 3:1 case (**Supplementary Fig. 7**). In the case of shorter filaments, less bending is induced in actin filaments via interactions with the boundary and, as such, bending that is stabilized by α-actinin to produce a delocalized actin center becomes rarer.

Sorting of α-actinin and fascin into different domains results in the formation of star-like structures.

To further understand the influence of spherical confinement, and the presence of both α-actinin and fascin on actin network architecture in GUVs, we encapsulated actin with different concentrations of both crosslinkers in GUVs and measured geometrical and physical characteristics of the structures from corresponding skeletonized actin networks. We first found that the GUV size-dependent architecture of actin bundles formed by α-actinin and fascin together followed a similar trend as α-actinin-actin structures **(Fig. 5a-c)**, namely, the propensity for actin ring formation reduces dramatically with increasing GUV size (**Fig. 5a**) yet it is not influenced by α-actinin concentration (**Fig. 5b**). The probability of the formation of single actin rings was lower compared to that in the presence of sole α-actinin irrespective of GUV size (78% (α-actinin and fascin) < 96% (α-actinin only) [small], 12% < 50% [medium], and 2% < 11% [large]) (see **Figs. 2b-c** and **5a-b**). Ring/network structures were present prevalently (~79%) in medium-sized GUVs, and sufficient space provided by large GUVs resulted in the formation of bundled networks (39% [large], 7% [medium], 1% [small]) (**Fig. 5a**). In medium and large GUVs, the portion of combined network and ring/network structures were the same irrespective of α-actinin concentration (**Fig.**

5c). In large GUVs, ~60% have networks forming aster-like or star-like structures, irrespective of α-actinin concentration **(Fig. 5d**). **Figure 5e** illustrates GUV size-dependent actin network architectures formed by α-actinin and fascin. Rings and aster-like structures around the GUV periphery can occasionally deform GUVs. Star-like actin structures typically appear at the center of large GUVs.

Observation of α-actinin-induced aggregation and packed bundling by fascin in aster- and star-like structures in the experiments directed us towards exploring a spontaneous sorting mechanism for arranging crosslinkers in the network in a GUV size-dependent manner. One line of evidence comes from the observation of larger actin aggregate sizes with increasing α-actinin concentration at fixed fascin concentration (**Fig. 6a**). This is evident from the medial plane of star-like structures and also linescan analysis of corresponding 3D maximum project images (**Fig. 6b**). Large GUVs with star-like actin bundle structures have semi-symmetric configuration as actin aggregates are positioned at the center of GUVs. This mirrors the structure exhibited by simulations in **Figure 4d**. Compared to symmetry breaking and polar configuration of aggregates in α-actinin-bundled actin structures, the addition of fascin significantly increased the probability of symmetric aggregate positioning to the center which may contribute to the formation of star-like structures in large GUVs **(Fig. 6c).** In this analysis, ~34% of encapsulated α-actinin-actin bundles and ~23% of encapsulated α-actinin-fascin-actin bundles did not form aggregates. In the presence of α-actinin and fascin, increasing GUV size also increased the possibility of aggregate localization at the GUV center (**Fig. 6d**). GUV size-dependent aggregate localization in the presence of both α-actinin and fascin is similar to droplet size-dependent localization of aggregates in encapsulated contractile actin networks, implying the existence of a force or inhibition mechanism against random attraction between actin bundles and the membrane[29]. As discussed earlier, α-actinin–bundled actin can bring the bundle in close proximity to the membrane thereby increasing the chance of stochastic bridging with the inner surface of the lipid bilayer. Fascin bundling activity, on the other hand, prevents bending and together with a large lumenal space can inhibit the engagement of the bundle to the membrane. This can explain disengagement of aggregates from the membrane in larger GUVs yet it does not enforce aggregate positioning at the GUV center. The higher fraction of aggregates found in the center of the α-actinin-fascin-actin GUVs and larger actin aggregates with increasing α-actinin suggest that cooperation among α-actinin bundlers enhances their recruitment and accumulation rather than colocalizing with fascin

in star-forming actin bundles. In such a scenario, fascin would dominate in actin networks outside of aggregates to form arrays of rigid actin bundles emanating from the aggregates, similar to the star-like structure with a dendritic actin core reconstituted in a membrane-free system[9].

α-Actinin increases rigidity of fascin-bundled actin due to increased crosslinker sorting.

This spontaneous sorting mechanism due to crosslinker competition leads to rigid actin bundles in the star-like structures. Since increasing α-actinin increased the size of actin aggregates in the GUV center, we hypothesize this may have an effect on the rigidity of fascin-bundled actin. To test this, we compared flexural rigidity of actin bundles by measuring bundle persistence length as a function of α-actinin concentration at a fixed fascin concentration. In order to eliminate the effect of membrane curvature on bundle bending, only lumenal actin bundles with no interaction or proximity to the membrane were considered. Actin crosslinking in GUVs typically resulted in the formation of structures that are connected with one or several joints per bundle (**Supplementary Fig. 8a**) with the exception of single rings and star-like structures which do not normally form joints outside aggregates. Because a crowded network can potentially contribute to an increase in the persistence length of actin filaments[40], we first showed that the formation of joints and connectivity between encapsulated actin bundles has negligible effect on their bending rigidity (L_p = 30 ± 10.7 μm [0-1 joint] and 36.1 ± 11.2 μm [2-4 joints]) (**Supplementary Fig. 8b**). These L_p values for α-actinin-actin bundles with α-actinin molar ratio of 0.1 explain their flexibility in large GUVs with radius greater than L_p and their inability to encircle around the membrane which, in turn, results in the formation of lumenal structures[28] (**Supplementary Fig. 8c**). An increase in the persistence length of crosslinked F-actin (L_p for actin filaments is ~ 10-17 μm), either in confinement or not, depends on both crosslinker type and concentration[46, 47]. Enforcing a confinement can also result in a reduction in polymer fluctuations and cause network stiffening[48]. The persistence length of actin bundles as a function of α-actinin concentration without and with fascin showed that the bending rigidity of actin bundles is larger in the presence of the both crosslinkers compared to α-actinin-bundled actin, as one would expect (L_p [fascin:α-actinin:actin] = 33.3 ± 10 μm [0:1:10], 54.2 ± 11.4 μm [1:1:10], and 39.3 ± 9 μm [0:3:10], 99.7 ± 15 μm [1:3:10]) (**Fig. 6e)**. Strikingly, the persistence length of α-actinin-fascin-actin bundles increased with increasing the molar ratio of α-actinin while at a fixed fascin concentration (L_p [fascin:α-

actinin:actin] = 54.2 ± 11.4 μm [1:1:10], 77.8 ± 19 μm [1:2:10], 99.7 ± 15 μm [1:3:10]) (**Fig. 6e**). Such an increase in bending rigidity is possible via a sorting mechanism where molecules of α-actinin favor their own type to assemble into a large domain at the GUV center, leaving tightly packed fascin-bundles radiating outwards. The presence of α-actinin in short-space bundles is energetically unfavorable due to its large size compared to fascin. This sorting mechanism has been shown to take place in 2D 2-filament actin bundles in bulk to minimize F-actin bending energy[12, 13]. Enhanced separation of cooperative α-actinin molecules from fascin domains at high α-actinin concentrations causes majority of α-actinin bundlers further accumulate and enhance network aggregation at the GUV center. Hence, these results support the existence of a competition-based mechanism for sorting of crosslinkers where higher concentrations of α-actinin enhance aggregation resulting in enhanced packed bundling via fascin. When we held α-actinin concentration constant while varying fascin concentration, the size and density of actin aggregates did not change **(Supplementary Fig. S9a-b)**. This provides further evidence that fascin does not have a tendency to co-localize with α-actinin in actin aggregates. Persistence length of α-actinin-fascin-actin star-forming bundles with a high α-actinin concentration remained high and did not further increase with fascin concentration (L_p [fascin:α-actinin:actin] = 99.7 ± 15 μm [1:3:10] and 97.6 ± 21.9 [3:3:10]) **(Supplementary Fig. S9c)**. This may be attributed to the geometrical limitations in persistence length measurement of actin bundles in a confined environment (see Methods). However, fascin-bundled actin in bulk at fascin molar ratio of 0.3 has a similar flexural rigidity (~100 μm)[47]. This further supports the segregation of α-actinin from fascin domains in star-like structures. The formation of long fascin domains by crosslinker sorting in large GUVs leaves α-actinin molecules to form actin clusters. The most energetically favorable network formation mechanism for α-actinin-induced clustering and fascin-induced radiation of rigid bundles is a competition-based crosslinker sorting which symmetrically positions actin aggregates at the GUV center allowing maximal elongation of actin bundles. The loss of transient contacts between α-actinin domains and the membrane in large GUVs contributes to the centering of the aggregates by such mechanism. As discussed, symmetric positioning of aggregate itself allows contact-less radiation and elongation of rigid actin bundles. Hence, the generation of star-like structures is the result of actin aggregation and radiation of rigid actin bundles both of which contribute to the positioning of one another.

Our results show that local concentration of crosslinkers and GUV size modulate the architecture of encapsulated actin bundles. Packed bundling activity of fascin and centering of α-actinin-induced aggregation, both promoted by spontaneous segregation of the crosslinkers, resulted in the formation of star-like structures in large GUVs. Boundary-imposed effect on protein sorting may be a general mechanism for cells to generate different dynamical steady states. Reconstitution of membrane proteins have revealed a protein size- and crowding-dependent protein exclusion machinery for membrane bending minimization and effective localization of membrane proteins at the membrane interface[49]. Moreover, binding energy of protein interactions can also act as the driving force for spontaneous segregation of membrane proteins at cellular junctions as shown in reconstituted immunological synapses[50]. Thus, boundary-imposed interactions present a simple yet efficient way of protein sorting in cellular processes which induce positioning and activation of proteins at specific sites enabling their localized functions.

Summary and outlook

In this study, we explored confined actin self-assembly induced by α-actinin and fascin. We found that crosslinked actin network architecture depends on GUV size and crosslinker concentration. Actin bundles merge into a single ring in smaller GUVs, whereas they form aster- and star-like structures in large GUVs. Network connectivity by α-actinin was sufficient for F-actin aggregation and GUV size-dependent formation of actin rings and asters. Our experiments and coarse-grained molecular dynamics simulation recapitulated star formation of α-actinin-fascin-actin bundles in confinement. We suggest that protein sorting enables symmetric positioning of α-actinin-actin aggregates and the formation of star-like fascin-bundled actin in large GUVs. Together with boundary-induced interactions due to confinement, the actin crosslinkers modulate actin self-organization into regular structures. Our results contribute to a better understanding of the effect of cell size on cytoskeletal organization in the cell and developing optimized platforms for cytoskeleton-based minimal cell design as well as the design of crosslinkers for engineered biopolymer networks. An interesting future direction is to implement models which, with the help of experiments, describe the influence of GUV hydrodynamics, membrane-structure interaction, and protein sorting on one another in

encapsulated connective and contractile actin networks, bringing us one step closer to a complete understanding of mechanical basis for self-segregation in cellular networks.

Methods

Proteins and Reagents

Actin was either purchased from Cytoskeleton Inc, USA or purified from rabbit skeletal muscle acetone powder (Pel-Freez Biologicals) as previously described[51]. ATTO 488 actin was purchased from Hypermol Inc, Germany. α-Actinin was purchased from Cytoskeleton Inc. Fascin was either purchased from Hypermol Inc, Germany, or purified from *E. coli* as Glutathione-S-Transferase (GST) fusion protein. For purification, BL21(DE3) *E. coli* cells was transformed with pGEX-4T-3 (GE Healthcare) containing the coding sequences of fascin. Cells were grown at 37 °C while shaking at 220 rpm until the OD_{600} reached 0.5 - 0.6. Protein expression was induced with 0.1 mM IPTG and cell cultures were incubated at 24 °C for 8 h. Cells were harvested by centrifugation at 4,000 x g for 15 min and washed with PBS once. Pellets were stored at -80 °C until the day of purification. Cell pellets were resuspended in lysis buffer (20 mM K-HEPES pH 7.5, 100 mM NaCl, 1 mM EDTA, 1 mM PMSF) and ruptured by sonication. Cell lysates were centrifuged at 75,000 x g for 25 min and supernatants were loaded on a GSTrap FF 1 mL column (GE Healthcare) using an AKTA Start purification system (GE Healthcare) at a flow rate of 1 mL/min. The column was washed with 15 mL washing buffer (20 mM K-HEPES pH 7.5, 100 mM NaCl) and the proteins were eluted with 5 mL elution buffer (washing buffer + 10 mM reduced L-glutathione). Purified products were dialyzed against 1 L PBS twice for 3 h and once overnight at 4 °C. Protein concentration was calculated by UV absorption using predicted molar extinction coefficients (ExPasy) of 110,700 $M^{-1}cm^{-1}$. Proteins were concentrated with Centricon filters (Merck-Millipore) when needed and/or diluted to a final concentration of 1 mg/mL in PBS.

GUV Generation and Microscopy

0.4 mM stock mixture of lipids containing 69.9% 1,2-dioleoyl-sn-glycero-3-phosphocholine (DOPC), 30% cholesterol, and 0.1% 1,2-dioleoyl-sn-glycero-3-

phosphoethanolamine-N-(lissamine rhodamine B sulfonyl) (Rhod-PE) in a 4:1 mixture of silicone oil and mineral oil was first made in a glass tube. The lipid/oil mixture could immediately be used or stored at 4 °C for a maximum of 2 days. DOPC, cholesterol, and Rhod-PE were purchased form Avanti Polar Lipids. Silicone oil and mineral oil were purchased from Sigma-Aldrich.

Next, 5 μM Actin (including 10% ATO 488 actin) in polymerization buffer (50 mM KCl, 2 mM $MgCl_2$, 0.2 mM $CaCl_2$, and 4.2 mM ATP in 15 mM Tris, pH 7.5) and 5% OptiPrep was prepared and kept in ice for 10 min. α-Actinin (0.5-1.5 μM) and/or fascin (0.5-1.5 μM) were then added to the sample. GUVs were generated in 20-30 s after the addition of crosslinkers.

GUVs were generated by a modification of the cDICE method[30] **(Supplementary Fig. S1a)**. A rotor chamber was 3D-printed with Clear resin by using a Form 3 3D printer (Formlabs) and mounted on the motor of a benchtop stir plate and rotated at 1,200 rpm (60 Hz). 0.71 mL aqueous outer solution (200 mM D-glucose matching the osmolarity of inner solution) and around 5 mL of lipid-in-oil dispersion are sequentially transferred into the rotating chamber. The difference in density between the two solutions results in the formation of two distinct layers with a vertical water/oil interface at their boundary. GUV generation was initiated by introduction of 15-20 μL inner solution carrying actin and actin-binding proteins in polymerization buffer containing 5% OptiPrep through a nozzle. Alternatively, a water-in-oil emulsion was first created by vigorously pipetting 15-20 μL of actin polymerization solution (including 5% OptiPrep) in 0.7 mL of lipid/oil mixture and the emulsion was pipetted into the rotating chamber. In either case, generated droplets travel through the lipid dispersion. Lipids are adsorbed at the droplet interface to form a monolayer. As the droplets cross the vertical water/oil interface, they acquire the second leaflet of the bilayer and get released in the outer solution as GUVs (bottom panel of **Supplementary Fig. S1a**).

The outer solution containing GUVs were transferred to a 96 well plate for microscopy. The presence of OptiPrep in GUV lumen increases GUV density and helps GUVs to sediment on the bottom of well plate. Plates were imaged 1 hour after the generation of GUVs unless otherwise mentioned. Images were captured using an oil immersion 60 x/1.4 NA Plan-Apochromat objective on an Olympus IX-81 inverted microscope equipped with a spinning disk confocal (Yokogawa CSU-X1), AOTF-controlled solid-state lasers (Andor Technology), and an iXON3 EMCCD camera (Andor Technology). Image acquisition was controlled by MetaMorph software

(Molecular Devices). Actin and lipid fluorescence images were taken with 488 nm laser excitation at exposure time of 350-500 ms and 561 nm laser excitation at exposure time of 20-25 ms respectively. A Semrock 25 nm quad-band band-pass filter was used as the emission filter. Z-stack image sequence of actin and lipids were taken with a step size of 0.5 μm.

Image Analysis

Image processing and image data analysis were performed using ImageJ/Fiji[52, 53], SOAX[32, 54], and custom MATLAB scripts **(Supplementary Fig. S2)**. All 3D images shown are maximum projections of z-tack confocal image sequences using 3D Project command in ImageJ/Fiji. For 3D characterization of actin bundle structures, we generated skeletonized models from regions of interest in actin images. In order to optimize the images for the identification of actin bundles, images were first preprocessed using Fiji (see Supplementary Methods). The structures from z-stack images are identified and extracted with SOAX source code[31, 32] by active contour methods.

SOAX program stores all the coordinates of snakes (skeletonized bundles) and joints in a .txt file. Custom MATLAB routines were written to reconstruct the text as a Chimera marker file, include a colormap for z coordinates, and save file as .cmm format. This process enabled UCSF Chimera[55] to read the file and provide a better 3D visualization of actin structures for selecting actin bundles and measuring parameters such as bundle length and radius of curvature, bond vectors, ring center of mass, and persistence length with MATLAB. GUV geometrical parameters such as diameter and membrane curvature were directly measured from lipid z-stack image sequences via ImageJ.

For more details regarding image processing and data analysis see Supplementary Methods.

Percentages and Probabilities

After taking Z-stack confocal image sequences of GUVs (561 nm) and encapsulated actin (488 nm), and image preprocessing of actin images, 3D reconstructed actin images were obtained via ImageJ brightest point projection using x- and y-axis, separately, as the axis of rotation. Both 3D reconstructed and z-stack images were used for determining the number of GUVs with

encapsulated actin bundles including those with certain structural phenotype (single ring, aster-like structures, and star-like structures). GUV diameters were measured by line scans from both raw actin images and GUVs. GUVs were then categorized as small (7-12 μm), medium (12-16 μm), and large (> 16 μm). The probability of the formation of an actin ring, ring/network, and network per GUV category per experiment were obtained by their count divided by the total number of captured GUVs in the specified category. The percentage of aster-like and star-like structures in large (or small/medium) GUVs per experiment were obtained by their count divided by the total number of captured large (or small/medium) GUVs with encapsulated actin bundles. The percentage of large (or small/medium) GUVs with actin aggregates positioned at the center (or periphery) were calculated by dividing their count by the total number of large (or small/medium) GUVs with encapsulated actin bundles. GUVs encapsulating fluorescent actin monomers with no sign of bundling activity were occasionally found in each population. These GUVs were not taken into account for probability distribution and percentage measurements.

Calculation of Persistence Length

Using coordinates of the bonds and joints of each skeletonized actin bundle, MATLAB scripts were written to calculate orientational correlation function, $\langle C(s)\rangle \equiv \langle\cos(\theta(s))\rangle$, as a function of arc length s along the contour length of selected actin bundles. $\cos(\theta(s))$ is the cosine of the angle between snake bond vectors separated by s. $\langle\ \rangle$ denotes ensemble average over all snake bonds as starting points. To avoid membrane curvature effect on persistence length measurement, selected actin bundles were among those with no interaction or proximity to the membrane. The lengths of selected actin bundles were $8 < L < 20$ μm.

Assuming that exponential decay of $\langle C(s)\rangle$ in 3D can be described as $\langle C(s)\rangle = C_0 e^{-s/L_p'}$, we fitted lines by linear regression to data points (s, $\langle \mathrm{Ln}(C(s))\rangle$) and determined the slope $-1/L_p'$ with L_p' denoting the effective persistence length[56, 57]. Among the selected skeletonized bundles, only those with coefficient of determination $R^2 > 0.8$ were picked for persistence length measurement. Absolute value of the intercept, $\mathrm{Ln}(|C_0|)$ for selected bundles was found to be around zero with a maximum of 0.03, underscoring the feasibility of assumption $C_0 = 1$ for persistence length measurement of actin bundles with length < 20 μm[47]. We did not find any correlation

between persistence length and length of the selected actin bundles for any given experimental condition.

Simulation Methods

To simulate cytoskeletal networks we turn to the AFINES simulation package which has been described previously[13, 43, 58] but will be summarized here. AFINES utilizes a coarse-grained description of components in order to efficiently simulate cytoskeletal dynamics. Specifically, filaments are rendered as $N + 1$ beads connected by N springs with $N - 1$ radial springs preventing the chain from being freely jointed. Similarly, crosslinkers are modeled as linear springs with heads (beads) on each end that can bind and unbind from filaments via a kinetic Monte Carlo scheme that preserves detailed balance. Molecular motors can also be described within this framework but will not be discussed here as they are not employed in this work.

The motion of filaments and crosslinkers evolve according to an overdamped Langevin dynamics in two dimensions. Because the simulation is two-dimensional while the system of interest is not and because we expect the behavior of the experiment to be dominated be network connectivity, we neglect excluded volume interactions between components. While this may lead to quantitative artifacts in the rate of structure formation, previous work has demonstrated that this model is effective in its description of a number of in vitro cytoskeletal systems.

In addition to the features detailed in previous work[13, 58], we have added a circular confinement potential U^{confine} to mimic the confinement inside the GUV, and an alignment potential U^{align} between actin filaments connected by fascin or α-actinin. The potential energies of filaments U_f and of crosslinkers U_{xl} are now

$$U_f = U_f^{\text{stretch}} + U_f^{\text{bend}} + U_f^{\text{confine}} \tag{1}$$

$$U_{xl} = U_{xl}^{\text{stretch}} + U_{xl}^{\text{bend}} + U_{xl}^{\text{bind}} + U_{xl}^{\text{confine}} + U_{xl}^{\text{align}} \tag{2}$$

For brevity we only describe the added terms. The confinement potential U^{confine} is implemented as a radial confinement potential starting at radius r_c with a tunable force constant k_c,

$$U^{\text{confine}} = \begin{cases} \frac{1}{2}k_c(r - r_c)^2 & if\ r \geq r_c \\ 0 & if\ r < r_c \end{cases} \tag{3}$$

where r is the distance of the filament or crosslinker bead from the center of the potential.

The alignment potential penalizes filaments which are not parallel in the case of fascin, and not parallel or antiparallel in the case of α-actinin. It is activated only when both heads of fascin or α-actinin are bound to actin filaments. For α-actinin, the potential is

$$U_{xl}^{\text{align}} = k_{xl}^{\text{A}}(1 - |cos\theta|) \tag{4}$$

and for fascin,

$$U_{xl}^{\text{align}} = k_{xl}^{\text{A}}(1 - cos\theta) \tag{5}$$

where k_{xl}^{A} is the penalty parameter for the angle θ between the springs of the bound filaments. Critically, this new term allows us to differentiate between a crosslinker that only binds to parallel filaments, such as fascin, and one that can bind either parallel or antiparallel filaments, such as α-actinin[13].

We utilize these new features and the existing functionality of the AFINES package to model α-actinin and fascin. One chief difference between the two crosslinkers is their respective lengths with fascin being almost a factor of 6 smaller[12]. As such we set the resting length of fascin to 0.06 and that of α-actinin to 0.36 in simulation units. Experimental measurements of the two crosslinkers' respective affinity for actin do not show significant differences [12] so the on and off rates for the respective crosslinkers are kept equal. That fascin bundles only parallel filaments and α-actinin has no preference between parallel and anti-parallel was captured through the U_{xl}^{align}potential. The penalty parameter k_{xl}^{A} as well as the crosslinker bending parameter k_{xl}^{B} were tuned such that the single component simulations for each crosslinker matched the experimental structures. The initial condition of the simulation was generated by centering each filament on the origin and assigning the angle between the filament 's barbed end and the x axis randomly. Once the angle was assigned, the filament was moved off of the origin by translating the bead positions

in x and y. The amount of displacement in each direction was drawn from a gaussian distribution centered at 0 with a standard deviation of 3 μm. Simulations ran for 500 seconds with a time step of 2×10^{-5} s. The updated version of AFINES including the new features described here as well as the full configuration files used to run these simulations and the script used to generate the initial conditions are available at https://github.com/Chatipat-and-Steven-friendship-forever/AFINES/tree/chatipat_integrate/crosslinker_sorting_in_GUVs.

Statistical Analysis

Error bars in experiments and simulations represent respectively the standard error of the mean and standard deviation value of the corresponding data. For probability and percentage measurements, the number of data points (n) was 3 (3 independent experiments). For persistence length measurements, n is the number of actin bundles persistence length of which were measured for each category. The reported *p* values are two-tail calculated by performing unpaired two-sample student t-test assuming unequal variances.

Author Contributions

YB and APL designed the experiments. YB conducted the experiments and analyzed the experimental data. AG, YB, and APL prepared purified proteins. YB, TL, and PS developed the data processing methods. ARD, GMH, SLR, and CA designed the modeling and simulations. SAR, and CL performed and analyzed the simulations. YB and APL wrote the manuscript. All authors discussed the results and commented on the manuscript.

Acknowledgements

We thank Giovanni Cardone of the MPI-B Image Facility for providing FIJI image processing tools. We also thank Sagardip Majumder and Hossein Moghimian for discussions and help with experimental procedures and data analysis. APL acknowledges support from National Science Foundation (1612917, 1844132, and 1817909). GMH is supported by a National Institute of Health grant R35-GM138312.

Competing Interests

The authors declare no competing interests.

Figure Captions:

Figure 1. The formation of distinct actin architectures in the presence of α-actinin and fascin. Representative 3D-reconstructed (left) and skeletonized (right) images from a confocal fluorescence image stack of 5 μM actin (10% ATTO 488 actin) bundled by 0.5 μM fascin and 1 μM of α-actinin in GUVs (composition: 69.9% DOPC, 30% cholesterol, and 0.1% rhodamine-PE). Yellow arrow denotes cluster of actin fluorescence in a star-like structure at the GUV center. White arrows denote peripheral cluster of actin fluorescence in aster-like structures. Color in the skeletonized image shows *z* position. Scale bar, 10 μm.

Figure 2. Organization of actin-α actinin networks depends on GUV size. a, Representative 3D reconstructed fluorescence confocal images of actin networks of different α-actinin to actin ratios (actin concentration at 5 μM). Actin bundles form networks in larger GUVs while they form a single ring in smaller GUVs. Dotted lines outline the boundary of vesicles. Scale bar, 10 μm. **b,** Cumulative probability (for all 3 α-actinin concentrations) of ring and network formation in GUVs with different sizes. **c, d,** Probability of the formation of rings and networks at different α-actinin concentrations. Error bars indicate standard error of the mean; n = 3 experiments. N_{GUVs} per experiment = [389 42 23, 67 45 38, 188 145 128] in order of ascending α-actinin concentration.

Figure 3. Aggregation of crosslinked actin by α-actinin and formation of aster-like structures. a, Representative 3D reconstructed image from confocal fluorescence images of 5 μM actin with α-actinin at α-actinin to actin ratio of 0.1 (top) and 0.3 (bottom) [M/M]. Crosslinked actin forms aster-like structures emanating from actin aggregates (arrows). **b**, Schematic representation of actin aggregation (green) to a focal point at the GUV periphery (pink) via cross-linking activity of α-actinin. Higher α-actinin concentration (right) leads to the formation of a larger and highly localized cluster of actin. **c**, Representative 3D (from 2 views of the same GUV) reconstructed image from confocal stack of fluorescence images of an encapsulated α-actinin/actin (3:10 [M/M]) network. High α-actinin concentration can induce the formation of dense aggregates at the GUV periphery. **d,** Aster formation probability of actin bundles depends on GUV size. The majority of actin bundles form asters in larger GUVs. Error bars indicate standard error of the

mean; n = 3 experiments. N_{GUVs} per experiment = [389 42 23, 67 45 38, 188 145 128] in order of ascending α-actinin concentration. **e**, Cumulative (3 experiments) proportion of peripheral (with all actin bundles elongated around GUV periphery) and lumenal (with at least one actin bundle elongated in GUV lumen) asters in large GUVs (diameter > 16 μm). At high α-actinin concentrations, the majority of actin bundles form peripheral asters. $N_{\text{Large GUVs with asters}}$ = [35, 14, 53] in order of ascending α-actinin concentration. **f,** Schematic summarizing the result of encapsulated actin network assembly by α-actinin (without fascin) in different sized vesicles.

Figure 4. Simulations of confined crosslinkers recapitulate star formation seen in experiment. a, Representative structure after 500 s of simulation of actin and "fascin" alone. Actin filaments are represented as red lines and fascin is shown as black dots. The border of the simulated vesicle is shown as a black circle. **b,** The final structure from a 500 s simulation of "α-actinin" and actin alone. α-Actinin is shown as turquoise dots. **c,** A typical structure at the end of a 500 s simulation with a 1:1 ratio of α-actinin to fascin. **d,** A typical structure at the end of a 500 s simulation with a 3:1 ratio of α-actinin to fascin. **e,** The probability density function (PDF) of actin beads with respect to their distance from the center of the simulation box for the 1:1 case shown in **(c)**. The solid line is the average of 5 independent simulations and the error bars represent one standard deviation. **f,** PDF of actin beads as a function of the distance from the center of the simulation box for the 3:1 case **(d)** constructed from 5 independent simulations. **g,** The root-mean-square distance (RMSD) of actin beads in the final structure from their initial positions in both the 1:1 and 3:1 cases. The height of the bar is the average of the RMSD over all trials and the error bars represent one standard deviation between the RMSD of each trial. **h,** Average bending potential energy in filaments in the 1:1 and 3:1 cases. The bar height is the average of the averages from each trial and the error bar is the standard deviation of the individual averages. The filament length in all cases is 30 μm.

Figure 5. GUV size-dependent formation of rings, aster-like, and star-like actin structures by α-actinin and fascin. a, Cumulative probability (α-actinin concentrations of 0.5, 1, and 1.5 μM with 0.5 μM fascin and 5 μM actin) of ring and network formation in GUVs with different sizes. **b, c,** Probability of the formation of rings **(b)** and networks **(c)** at different α-actinin concentrations

as a function of GUV diameter. **d**, Probability of aster formation (including stars) in the presence of fascin and α-actinin. Aster formation depends on GUV size but not α-actinin concentration. Fascin/actin, 0.1 (M/M). All error bars indicate standard error of the mean; n = 3 experiments. N_{GUVs} per experiment = [101 98 29, 147 58 71, 137 82 24] in order of ascending α-actinin concentration. **e**, Schematic representation of GUV-size dependent actin networks assembled by α-actinin and fascin.

Figure 6. Flexural rigidity of actin bundles and GUV-size dependent localization of F-actin aggregates in the presence of α-actinin and fascin suggests crosslinker sorting and domain formation. a, Representative 2D (left) confocal fluorescence images of actin networks shown by arrows (3D reconstructed image, middle) along with skeletonized (right) image of the GUV populations. α-actinin, 0.5 μM (top), 1.5 μM (bottom). Fascin, 0.5 μM. Actin, 5 μM. Scale bar, 10 μm. **b,** Actin fluorescence intensity along the dashed lines drawn across the two GUVs in (a). **c**, Cumulative probability (for all α-actinin concentrations) of the aggregation of crosslinked actin with/without fascin in GUVs with diameter > 20 μm. α-actinin-fascin-actin bundles tend to shift cluster localization from periphery to the center of GUVs. $N_{GUVs>20\ \mu m}$ = 167 [87 (α-actinin), 80 (α-actinin+fascin)]. **d**, Cumulative probability (for all α-actinin concentrations) of the aggregation of crosslinked actin in large GUVs in the presence of both α-actinin and fascin. Larger GUVs facilitate centering of aggregates. $N_{analyzed\ GUVs>16\ \mu m}$ = 87 (61 [17-24 μm], 26 [>24 μm]). **e,** Persistence length of actin bundles without and with fascin (fascin/actin, 0.1 [M/M]) at different α-actinin/actin ratios indicated. $N_{bundles}$ = [22 14 17 14 26] in order of x-axis categories; 3 GUVs per category.

References

1. Fletcher DA, Mullins RD. Cell mechanics and the cytoskeleton. *Nature* 2010, **463**(7280)**:** 485-492.

2. Blanchoin L, Boujemaa-Paterski R, Sykes C, Plastino J. Actin dynamics, architecture, and mechanics in cell motility. *Physiol. Rev.* 2014, **94**(1)**:** 235-263.

3. Fujiwara K, Porter ME, Pollard TD. Alpha-actinin localization in the cleavage furrow during cytokinesis. *J. Cell Biol.* 1978, **79**(1)**:** 268-275.

4. Yin W, Li W, Li Q, Liu Y, Liu J, Ren M*, et al.* Real-time imaging of individual virion-triggered cortical actin dynamics for human immunodeficiency virus entry into resting CD4 T cells. *Nanoscale* 2020, **12**(1)**:** 115-129.

5. Jacquemet G, Hamidi H, Ivaska J. Filopodia in cell adhesion, 3D migration and cancer cell invasion. *Curr. Opin. Cell Biol.* 2015, **36:** 23-31.

6. Machesky LM, Li A. Fascin: Invasive filopodia promoting metastasis. *Commun. Integr. Biol.* 2010, **3**(3)**:** 263-270.

7. Burke TA, Christensen JR, Barone E, Suarez C, Sirotkin V, Kovar DR. Homeostatic actin cytoskeleton networks are regulated by assembly factor competition for monomers. *Curr. Biol.* 2014, **24**(5)**:** 579-585.

8. Christensen JR, Hocky GM, Homa KE, Morganthaler AN, Hitchcock-DeGregori SE, Voth GA*, et al.* Competition between Tropomyosin, Fimbrin, and ADF/Cofilin drives their sorting to distinct actin filament networks. *Elife* 2017, **6:** e23152.

9. Haviv L, Brill-Karniely Y, Mahaffy R, Backouche F, Ben-Shaul A, Pollard TD*, et al.* Reconstitution of the transition from lamellipodium to filopodium in a membrane-free system. *Proc. Natl Acad. Sci. U S A* 2006, **103**(13)**:** 4906-4911.

10. Vignjevic D, Yarar D, Welch MD, Peloquin J, Svitkina T, Borisy GG. Formation of filopodia-like bundles in vitro from a dendritic network. *J. Cell Biol.* 2003, **160**(6)**:** 951-962.

11. Brieher WM, Coughlin M, Mitchison TJ. Fascin-mediated propulsion of Listeria monocytogenes independent of frequent nucleation by the Arp2/3 complex. *J. Cell Biol.* 2004, **165**(2)**:** 233-242.

12. Winkelman JD, Suarez C, Hocky GM, Harker AJ, Morganthaler AN, Christensen JR*, et al.* Fascin-and α-actinin-bundled networks contain intrinsic structural features that drive protein sorting. *Curr. Biol.* 2016, **26**(20)**:** 2697-2706.

13. Freedman SL, Suarez C, Winkelman JD, Kovar DR, Voth GA, Dinner AR*, et al.* Mechanical and kinetic factors drive sorting of F-actin cross-linkers on bundles. *Proc. Natl Acad. Sci. U S A* 2019, **116**(33)**:** 16192-16197.

14. Co C, Wong DT, Gierke S, Chang V, Taunton J. Mechanism of actin network attachment to moving membranes: barbed end capture by N-WASP WH2 domains. *Cell* 2007, **128**(5)**:** 901-913.

15. Ganzinger KA, Vogel SK, Mücksch J, Blumhardt P, Schwille P. Myosin-II activity generates a dynamic steady state with continuous actin turnover in a minimal actin cortex. *J. Cell Sci.* 2019, **132**(4).

16. Liu AP, Fletcher DA. Actin polymerization serves as a membrane domain switch in model lipid bilayers. *Biophys. J.* 2006, **91**(11)**:** 4064-4070.

17. Liu AP, Richmond DL, Maibaum L, Pronk S, Geissler PL, Fletcher DA. Membrane-induced bundling of actin filaments. *Nat. Phys.* 2008, **4**(10)**:** 789-793.

18. Simon C, Kusters R, Caorsi V, Allard A, Abou-Ghali M, Manzi J*, et al.* Actin dynamics drive cell-like membrane deformation. *Nat. Phys.* 2019, **15**(6)**:** 602-609.

19. Köster DV, Husain K, Iljazi E, Bhat A, Bieling P, Mullins RD*, et al.* Actomyosin dynamics drive local membrane component organization in an in vitro active composite layer. *Proc. Natl Acad. Sci. U S A* 2016, **113**(12)**:** E1645-E1654.

20. Malik-Garbi M, Ierushalmi N, Jansen S, Abu-Shah E, Goode BL, Mogilner A*, et al.* Scaling behaviour in steady-state contracting actomyosin networks. *Nat. Phys.* 2019, **15**(5)**:** 509-516.

21. Bashirzadeh Y, Liu AP. Encapsulation of the cytoskeleton: towards mimicking the mechanics of a cell. *Soft Matter* 2019, **15**(42)**:** 8425-8436.

22. Lee KY, Park S-J, Lee KA, Kim S-H, Kim H, Meroz Y*, et al.* Photosynthetic artificial organelles sustain and control ATP-dependent reactions in a protocellular system. *Nat. Biotechnol.* 2018, **36**(6)**:** 530-535.

23. Vogel SK, Wölfer C, Ramirez-Diaz DA, Flassig RJ, Sundmacher K, Schwille P. Symmetry breaking and emergence of directional flows in minimal actomyosin cortices. *Cells* 2020, **9**(6)**:** 1432.

24. Litschel T, Kelley CF, Holz D, Koudehi MA, Vogel SK, Burbaum L*, et al.* Reconstitution of contractile actomyosin rings in vesicles. *BioRxiv* 2020.

25. Baumann H, Surrey T. Motor-mediated cortical versus astral microtubule organization in lipid-monolayered droplets. *J. Biol. Chem.* 2014, **289**(32)**:** 22524-22535.

26. Juniper MP, Weiss M, Platzman I, Spatz JP, Surrey T. Spherical network contraction forms microtubule asters in confinement. *Soft Matter* 2018, **14**(6)**:** 901-909.

27. Colin A, Singaravelu P, Théry M, Blanchoin L, Gueroui Z. Actin-network architecture regulates microtubule dynamics. *Curr. Biol.* 2018, **28**(16)**:** 2647-2656. e2644.

28. Miyazaki M, Chiba M, Eguchi H, Ohki T, Ishiwata Si. Cell-sized spherical confinement induces the spontaneous formation of contractile actomyosin rings in vitro. *Nat. Cell Biol.* 2015, **17**(4)**:** 480-489.

29. Ierushalmi N, Malik-Garbi M, Manhart A, Shah EA, Goode BL, Mogilner A*, et al.* Centering and symmetry breaking in confined contracting actomyosin networks. *Elife* 2020, **9:** e55368.

30. Abkarian M, Loiseau E, Massiera G. Continuous droplet interface crossing encapsulation (cDICE) for high throughput monodisperse vesicle design. *Soft Matter* 2011, **7**(10)**:** 4610-4614.

31. Xu T, Vavylonis D, Tsai F-C, Koenderink GH, Nie W, Yusuf E*, et al.* SOAX: a software for quantification of 3D biopolymer networks. *Sci. Rep.* 2015, **5:** 9081.

32. Xu T, Vavylonis D, Huang X. 3D actin network centerline extraction with multiple active contours. *Med. Image Anal.* 2014, **18**(2)**:** 272-284.

33. Koenderink GH, Paluch EK. Architecture shapes contractility in actomyosin networks. *Curr. Opin. Cell Biol.* 2018, **50:** 79-85.

34. e Silva MS, Depken M, Stuhrmann B, Korsten M, MacKintosh FC, Koenderink GH. Active multistage coarsening of actin networks driven by myosin motors. *Proc. Natl Acad. Sci. U S A* 2011, **108**(23)**:** 9408-9413.

35. Adeli Koudehi M, Rutkowski DM, Vavylonis D. Organization of associating or crosslinked actin filaments in confinement. *Cytoskeleton* 2019, **76**(11-12)**:** 532-548.

36. Lieleg O, Schmoller KM, Cyron CJ, Luan Y, Wall WA, Bausch AR. Structural polymorphism in heterogeneous cytoskeletal networks. *Soft Matter* 2009, **5**(9)**:** 1796-1803.

37. Tempel M, Isenberg G, Sackmann E. Temperature-induced sol-gel transition and microgel formation in alpha -actinin cross-linked actin networks: A rheological study. *Phys Rev E Stat Phys Plasmas Fluids Relat Interdiscip Topics* 1996, **54**(2)**:** 1802-1810.

38. Thoresen T, Lenz M, Gardel ML. Reconstitution of contractile actomyosin bundles. *Biophys. J.* 2011, **100**(11)**:** 2698-2705.

39. Wollrab V, Belmonte JM, Baldauf L, Leptin M, Nédeléc F, Koenderink GH. Polarity sorting drives remodeling of actin-myosin networks. *J. Cell Sci.* 2019, **132**(4).

40. Murrell MP, Gardel ML. F-actin buckling coordinates contractility and severing in a biomimetic actomyosin cortex. *Proc. Natl Acad. Sci. U S A* 2012, **109**(51)**:** 20820-20825.

41. Ennomani H, Letort G, Guérin C, Martiel J-L, Cao W, Nédélec F*, et al.* Architecture and connectivity govern actin network contractility. *Curr. Biol.* 2016, **26**(5)**:** 616-626.

42. Wang S, Wolynes PG. Tensegrity and motor-driven effective interactions in a model cytoskeleton. *J. Chem. Phys.* 2012, **136**(14)**:** 145102.

43. Freedman SL, Hocky GM, Banerjee S, Dinner AR. Nonequilibrium phase diagrams for actomyosin networks. *Soft Matter* 2018, **14**(37)**:** 7740-7747.

44. Senger F, Pitaval A, Ennomani H, Kurzawa L, Blanchoin L, Théry M. Spatial integration of mechanical forces by α-actinin establishes actin network symmetry. *J. Cell Sci.* 2019, **132**(22).

45. Sakamoto R, Tanabe M, Hiraiwa T, Suzuki K, Ishiwata Si, Maeda YT*, et al.* Tug-of-war between actomyosin-driven antagonistic forces determines the positioning symmetry in cell-sized confinement. *Nat. Commun.* 2020, **11**(1)**:** 1-13.

46. Claessens MM, Bathe M, Frey E, Bausch AR. Actin-binding proteins sensitively mediate F-actin bundle stiffness. *Nat. Mater.* 2006, **5**(9)**:** 748-753.

47. Takatsuki H, Bengtsson E, Mansson A. Persistence length of fascin-cross-linked actin filament bundles in solution and the in vitro motility assay. *Biochim. Biophys. Acta* 2014, **1840**(6)**:** 1933-1942.

48. Claessens M, Tharmann R, Kroy K, Bausch A. Microstructure and viscoelasticity of confined semiflexible polymer networks. *Nat. Phys.* 2006, **2**(3)**:** 186-189.

49. Schmid EM, Bakalar MH, Choudhuri K, Weichsel J, Ann HS, Geissler PL*, et al.* Size-dependent protein segregation at membrane interfaces. *Nat. Phys.* 2016, **12**(7)**:** 704-711.

50. James JR, Vale RD. Biophysical mechanism of T-cell receptor triggering in a reconstituted system. *Nature* 2012, **487**(7405)**:** 64-69.

51. Pardee JD, Aspudich J. [18] Purification of muscle actin. *Meth. Enzymol*, vol. 85. Elsevier, 1982, pp 164-181.

52. Schneider CA, Rasband WS, Eliceiri KW. NIH Image to ImageJ: 25 years of image analysis. *Nat. Methods* 2012, **9**(7)**:** 671-675.

53. Schindelin J, Arganda-Carreras I, Frise E, Kaynig V, Longair M, Pietzsch T*, et al.* Fiji: an open-source platform for biological-image analysis. *Nat. Methods* 2012, **9**(7)**:** 676-682.

54. Xu T, Vavylonis D, Tsai F-C, Koenderink GH, Nie W, Yusuf E*, et al.* SOAX: A software for quantification of 3D biopolymer networks. *Sci. Rep.* 2015, **5**(1)**:** 9081.

55. Pettersen EF, Goddard TD, Huang CC, Couch GS, Greenblatt DM, Meng EC*, et al.* UCSF Chimera--a visualization system for exploratory research and analysis. *J. Comput. Chem.* 2004, **25**(13)**:** 1605-1612.

56. Hsu H-P, Paul W, Binder K. Standard definitions of persistence length do not describe the local "intrinsic" stiffness of real polymer chains. *Macromolecules* 2010, **43**(6)**:** 3094-3102.

57. Ullner M, Woodward CE. Orientational correlation function and persistence lengths of flexible polyelectrolytes. *Macromolecules* 2002, **35**(4)**:** 1437-1445.

58. Freedman SL, Banerjee S, Hocky GM, Dinner AR. A Versatile Framework for Simulating the Dynamic Mechanical Structure of Cytoskeletal Networks. *Biophys J* 2017, **113**(2)**:** 448-460.

Figure 1

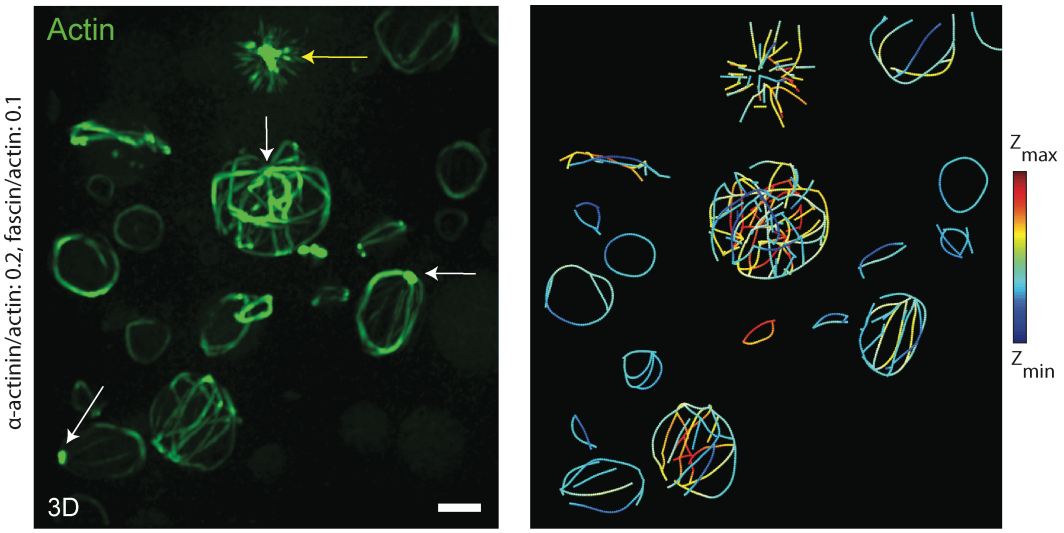

Figure 2

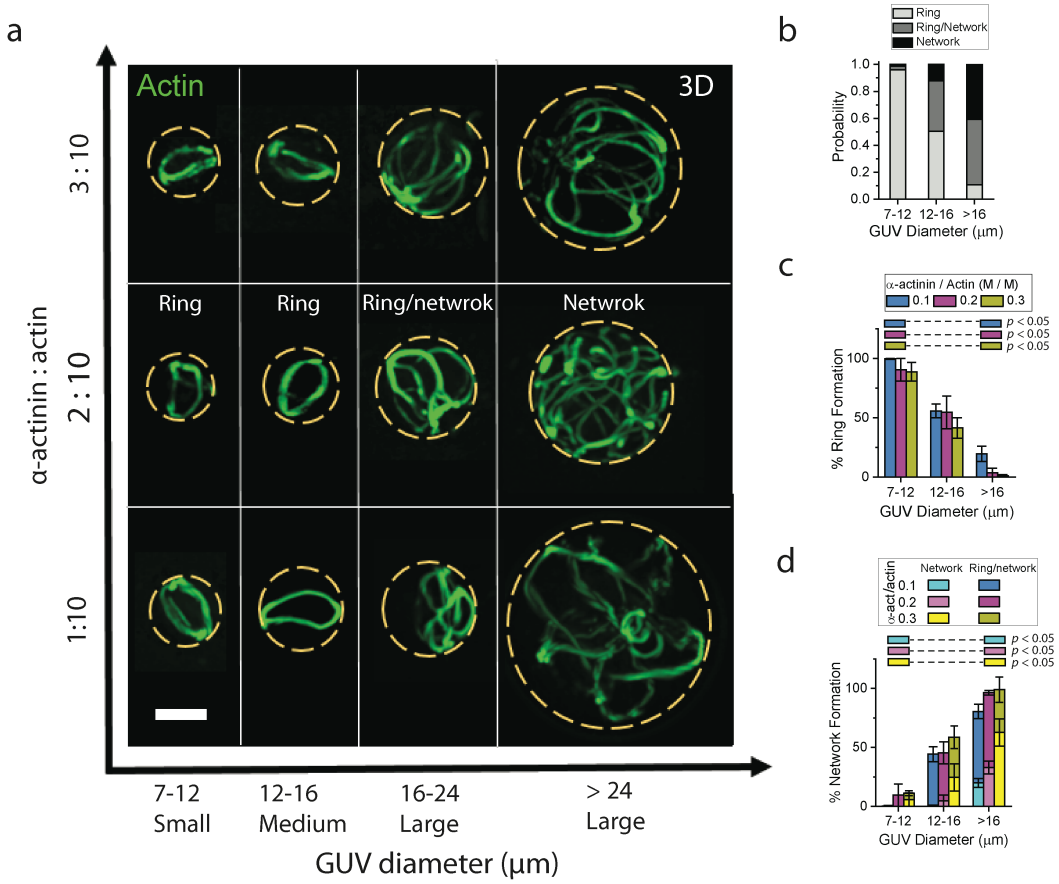
a
Actin
3D
Ring
Ring
Ring/netwrok
Netwrok
3 : 10
2 : 10
1:10
α-actinin : actin
7-12
Small
12-16
Medium
16-24
Large
> 24
Large
GUV diameter (μm)
b
Ring
Ring/Network
Network
Probability
GUV Diameter (μm)
c
α-actinin / Actin (M / M)
0.1
0.2
0.3
% Ring Formation
GUV Diameter (μm)
d
α-act/actin
Network
Ring/network
% Network Formation
GUV Diameter (μm)

Figure 3

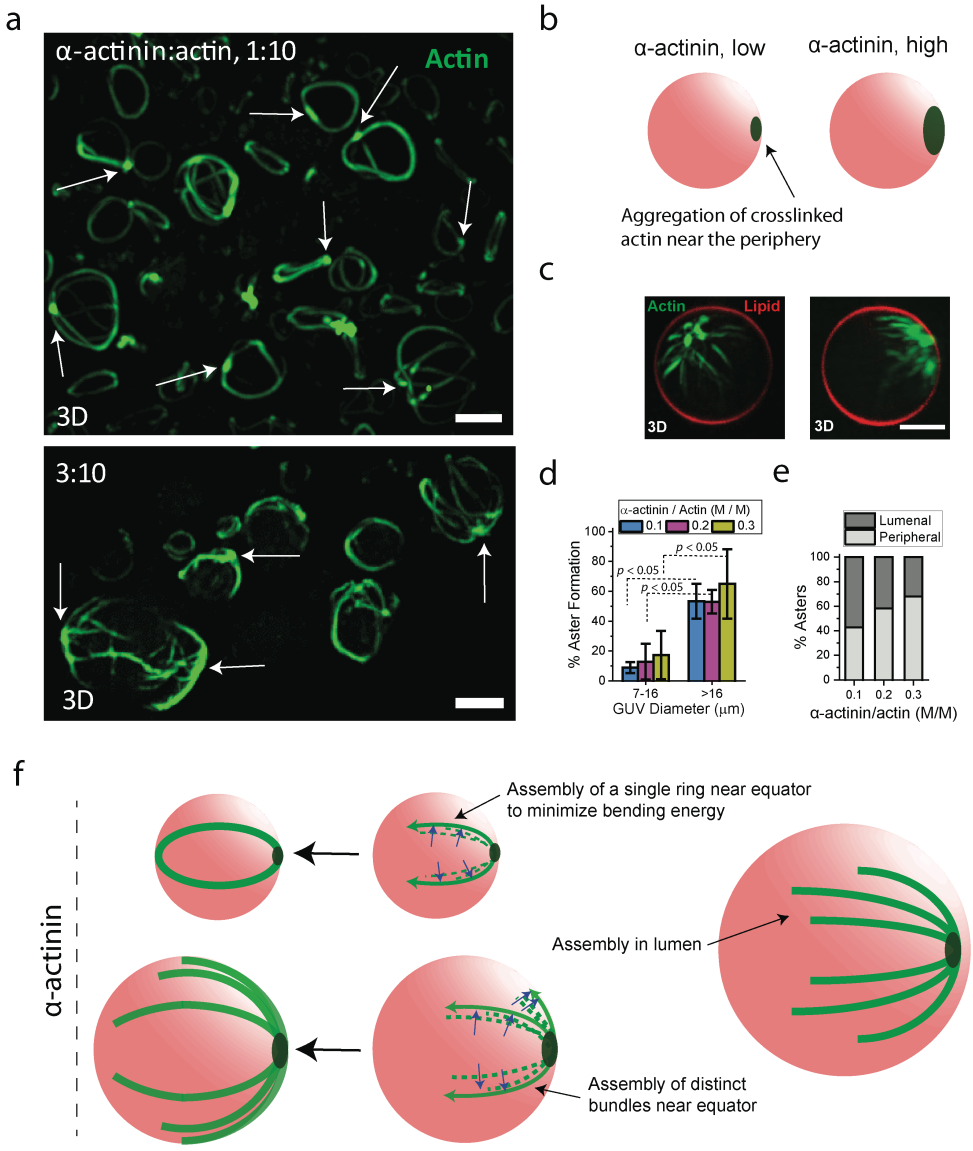
a
α-actinin:actin, 1:10
Actin
3D
3:10
3D
b
α-actinin, low
α-actinin, high
Aggregation of crosslinked actin near the periphery
c
Actin
Lipid
3D
3D
d
α-actinin / Actin (M / M)
0.1
0.2
0.3
% Aster Formation
p < 0.05
p < 0.05
p < 0.05
7-16
>16
GUV Diameter (μm)
e
Lumenal
Peripheral
% Asters
0.1
0.2
0.3
α-actinin/actin (M/M)
f
α-actinin
Assembly of a single ring near equator to minimize bending energy
Assembly in lumen
Assembly of distinct bundles near equator

Figure 4

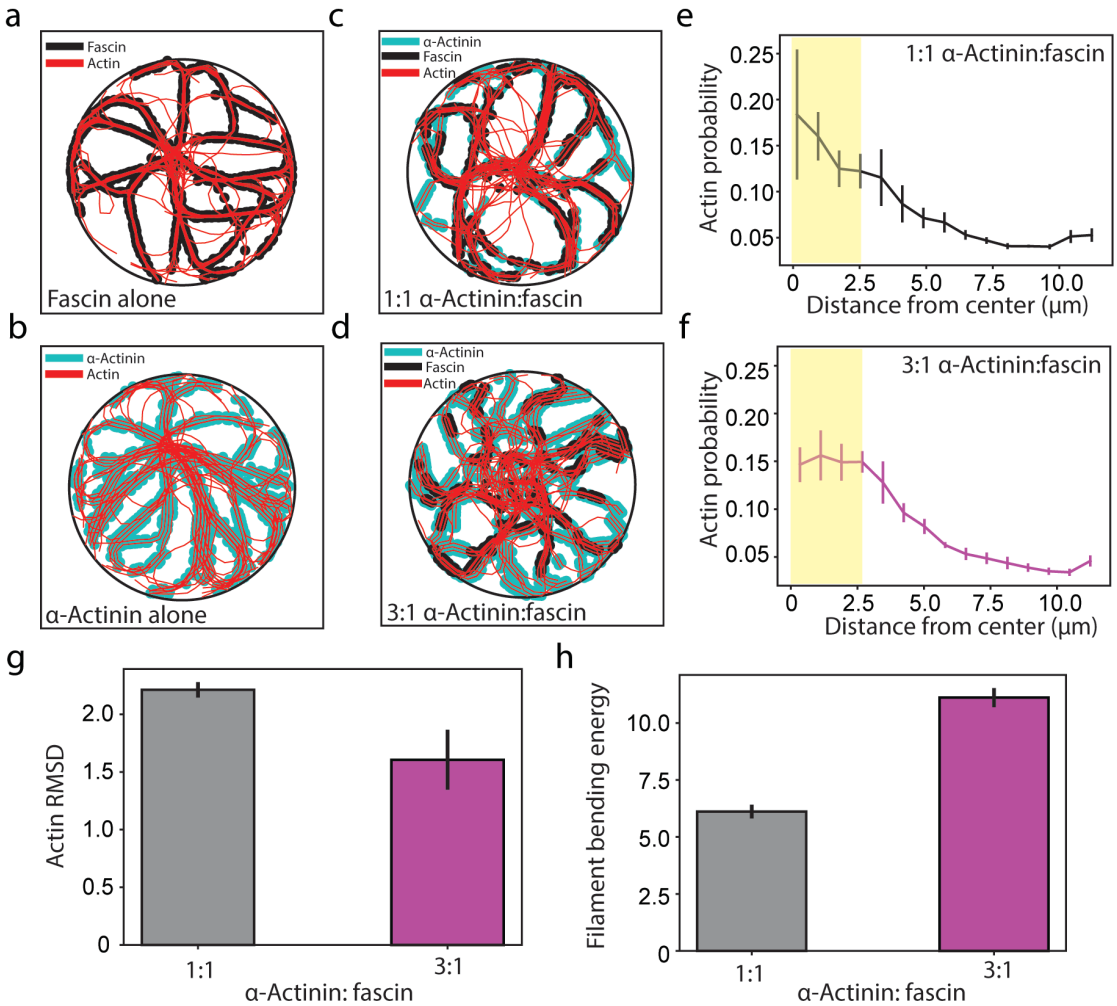
a
Fascin
Actin
Fascin alone
b
α-Actinin
Actin
α-Actinin alone
c
α-Actinin
Fascin
Actin
1:1 α-Actinin:fascin
d
α-Actinin
Fascin
Actin
3:1 α-Actinin:fascin
e
1:1 α-Actinin:fascin
Actin probability
0.25
0.20
0.15
0.10
0.05
0
2.5
5.0
7.5
10.0
Distance from center (μm)
f
3:1 α-Actinin:fascin
Actin probability
0.25
0.20
0.15
0.10
0.05
0
2.5
5.0
7.5
10.0
Distance from center (μm)
g
Actin RMSD
2.0
1.5
1.0
0.5
0
1:1
3:1
α-Actinin: fascin
h
Filament bending energy
10.0
7.5
5.0
2.5
0
1:1
3:1
α-Actinin: fascin

Figure 5

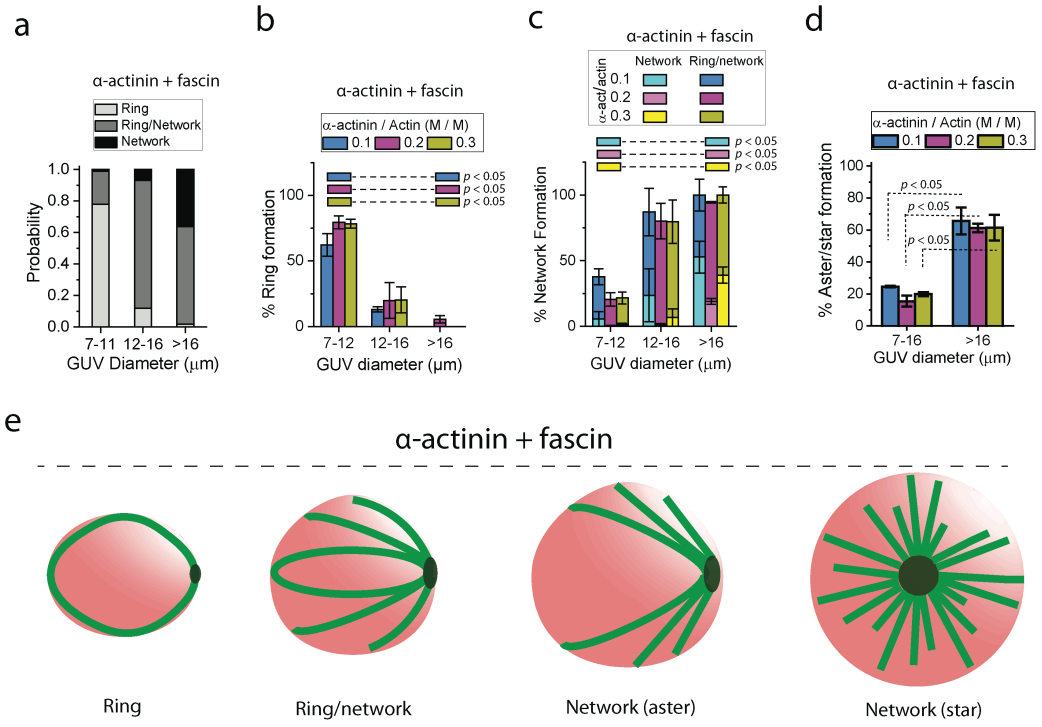
a
α-actinin + fascin
Ring
Ring/Network
Network
Probability
1.0
0.8
0.6
0.4
0.2
0.0
7-11
12-16
>16
GUV Diameter (μm)
b
α-actinin + fascin
α-actinin / Actin (M / M)
0.1
0.2
0.3
p < 0.05
p < 0.05
p < 0.05
% Ring formation
100
50
0
7-12
12-16
>16
GUV diameter (μm)
c
α-actinin + fascin
Network
Ring/network
α-act/actin
0.1
0.2
0.3
p < 0.05
p < 0.05
p < 0.05
% Network Formation
100
50
0
7-12
12-16
>16
GUV diameter (μm)
d
α-actinin + fascin
α-actinin / Actin (M / M)
0.1
0.2
0.3
p < 0.05
p < 0.05
p < 0.05
% Aster/star formation
100
80
60
40
20
0
7-16
>16
GUV diameter (μm)
e
α-actinin + fascin
Ring
Ring/network
Network (aster)
Network (star)

Figure 6

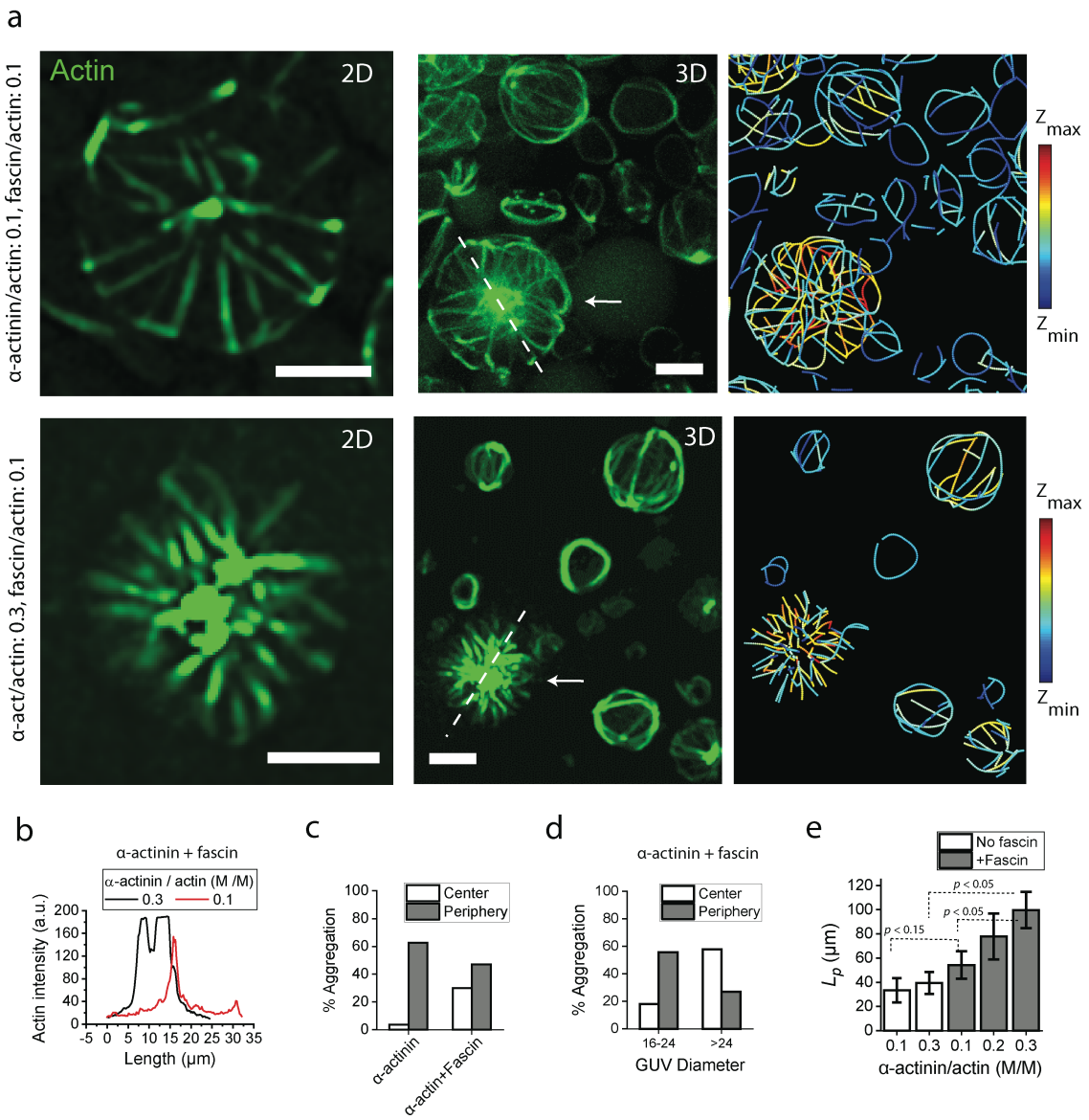
a
α-actinin/actin: 0.1, fascin/actin: 0.1
Actin
2D
3D
Z max
Z min
α-act/actin: 0.3, fascin/actin: 0.1
2D
3D
Z max
Z min
b
α-actinin + fascin
α-actinin / actin (M /M)
0.3
0.1
Actin intensity (a.u.)
Length (μm)
c
Center
Periphery
% Aggregation
α-actinin
α-actin+Fascin
d
α-actinin + fascin
Center
Periphery
% Aggregation
16-24
>24
GUV Diameter
e
No fascin
+Fascin
p < 0.05
p < 0.05
p < 0.15
L_p (μm)
0.1 0.3 0.1 0.2 0.3
α-actinin/actin (M/M)